Unravelling the effect of nitrogen on the morphological evolution of thin silver films on weakly-interacting substrates

K. Sarakinos, David Babonneau, J. Ramade, Y. Robin, K. Solanki, K. Mizohata, V. Tuboltsev, N. Pliatsikas, B. Krause, G. Abadias

▶ **To cite this version:**

K. Sarakinos, David Babonneau, J. Ramade, Y. Robin, K. Solanki, et al.. Unravelling the effect of nitrogen on the morphological evolution of thin silver films on weakly-interacting substrates. Applied Surface Science, 2024, 649, pp.159209. 10.1016/j.apsusc.2023.159209 . hal-04367116

HAL Id: hal-04367116
https://hal.science/hal-04367116v1

Submitted on 29 Dec 2023

HAL is a multi-disciplinary open access archive for the deposit and dissemination of scientific research documents, whether they are published or not. The documents may come from teaching and research institutions in France or abroad, or from public or private research centers.

L'archive ouverte pluridisciplinaire **HAL**, est destinée au dépôt et à la diffusion de documents scientifiques de niveau recherche, publiés ou non, émanant des établissements d'enseignement et de recherche français ou étrangers, des laboratoires publics ou privés.

Distributed under a Creative Commons Attribution 4.0 International License

Applied Surface Science 649 (2024) 159209

Contents lists available at ScienceDirect

Applied Surface Science

journal homepage: www.elsevier.com/locate/apsusc

Full Length Article

Unravelling the effect of nitrogen on the morphological evolution of thin silver films on weakly-interacting substrates

K. Sarakinos [a,b,*], D. Babonneau [c], J. Ramade [c], Y. Robin [c], K. Solanki [c], K. Mizohata [a], V. Tuboltsev [a], N. Pliatsikas [d], B. Krause [e], G. Abadias [c]

[a] Department of Physics, University of Helsinki, P.O. Box 43, FI-00014 Helsinki, Finland
[b] KTH Royal Institute of Technology, Department of Physics, Roslagstullsbacken 21, 114 21 Stockholm, Sweden
[c] Université de Poitiers, ISAE-ENSMA, CNRS, PPRIME, Poitiers, France
[d] Department of Physics, Aristotle University of Thessaloniki, GR-54124 Thessaloniki, Greece
[e] Institute for Photon Science and Synchrotron Radiation, Karlsruhe Institute of Technology, D-76344 Eggenstein-Leopoldshafen, Germany

ARTICLE INFO

Keywords:
Thin film nucleation and growth
In situ diagnostics
Growth manipulation
Weakly-interacting film-substrate systems

ABSTRACT

We study the effect of nitrogen on the morphological evolution of thin silver (Ag) films deposited on weakly-interacting amorphous carbon (a-C) and silicon oxide (SiO_x) surfaces. Films are synthesized at a deposition rate of $0.1\,nm{\cdot}s^{-1}$ by direct current magnetron sputtering (DCMS), high power impulse magnetron sputtering (HiPIMS), and electron-beam evaporation (EBE). We monitor growth *in situ* and in real time by measuring the evolution of film stress and optical properties, complemented by *ex situ* analyses of discontinuous-layer morphologies, film crystal structure, and film composition. We find that addition of molecular nitrogen (N_2) to the plasmagenic gas (Ar) during DCMS and HiPIMS promotes a two-dimensional (2D) morphology. Concurrently, EBE-deposited films exhibit a significantly more pronounced three-dimensional morphological evolution, independently from the gas atmosphere composition. We argue that the 2D morphology in DCMS- and HiPIMS-grown films is enhanced due to incorporation of atomic nitrogen (N)—result of plasma-induced N_2 dissociation—that hinders island reshaping during coalescence. This mechanism is not active during EBE due to the absence of energetic plasma electrons driving N_2 dissociation. The overall results of the study show that accurate control of vapor-phase chemistry is of paramount importance when using gaseous species as agents for manipulating growth in weakly-interacting film-substrate systems.

1. Introduction

Thin noble-metal films that serve as multifunctional contacts on oxides, semiconductors, and van-der-Waals materials, are a key component in a wide array of heterostructure devices [1–9]. These films are typically synthesized via condensation from the vapor phase, and the resulting device performance crucially depends on film morphology: in some cases, a flat two-dimensional (2D) layer that wets the underlying substrate in a complete and uniform fashion is essential [1,2], while in other cases device functionality requires that the deposited layer self-assembles in three-dimensional (3D) nanostructures with well-defined sizes and shapes [5]. Achieving such morphology control can be challenging, as noble-metal atoms may exhibit a weak interaction (i.e., bond strength) with oxide/semiconductor/van-der-Waals substrate atoms, leading to an uncontrolled formation of 3D nanoscale islands [1,10].

Vapor-based film synthesis is a far-from-equilibrium process during which morphological evolution primarily depends on kinetics of atomic-scale processes operating at various formation stages [11]. By altering deposition parameters (e.g., substrate temperature and vapor arrival rate) and/or deploying minority metal [12–15] and gaseous species [16–21] at the film growth front, the rates of such structure-forming processes can be modified, and thereby the film morphology can be manipulated. In particular, recent studies [16,17,19] have shown that the tendency towards 3D morphological evolution of magnetron-sputtered silver (Ag) layers on weakly-interacting zinc oxide (ZnO) and silicon oxide (SiO_x) substrates can be suppressed—leading to effectively smoother film surfaces—by introducing molecular nitrogen (N_2) to the plasmagenic gas. Moreover, it has been suggested that N_2 promotes 2D morphology by delaying the process of island reshaping during coalescence, which favors in-plane cluster expansion at the

* Corresponding author at: Department of Physics, University of Helsinki, P.O. Box 43, FI-00014 Helsinki, Finland.
E-mail address: kostas.sarakinos@helsinki.fi (K. Sarakinos).

https://doi.org/10.1016/j.apsusc.2023.159209
Received 11 October 2023; Received in revised form 14 December 2023; Accepted 23 December 2023
Available online 25 December 2023
0169-4332/© 2023 The Author(s). Published by Elsevier B.V. This is an open access article under the CC BY license (http://creativecommons.org/licenses/by/4.0/).

expense of out-of-plane growth [17,19]. However, the detailed pathways by which N_2 affects material redistribution during coalescence and influences the island shape and the overall film morphology are not understood, while possible effects on other film-formation stages (e.g., nucleation) have not been ruled out. This knowledge gap is further exacerbated by the fact that adsorption, desorption, and diffusion of nitrogen species on the growing surface may be affected by their chemical nature—in magnetron sputtering discharges nitrogen exists in both molecular (N_2) and atomic (N) form [22,23]—and their interactions with energetic ionized plasma species that are inherent to magnetron sputtering.

In the present work, we study nitrogen-modified growth of Ag on weakly-interacting amorphous carbon (a-C) and SiO_x substrates by three deposition methods: direct current magnetron sputtering (DCMS), high-power impulse magnetron sputtering (HiPIMS), and electron-beam evaporation (EBE). These methods enable us to access a wide range of process conditions with respect to energies and ionization degrees of film-forming and gas species, as well as the propensity for N production via N_2 dissociation. We monitor film growth in real time using *in situ* wafer curvature measurements and surface differential reflectance spectroscopy (SDRS), from which we find that the addition of N_2 to DCMS and HiPIMS Ar-based discharges leads to formation of continuous layers at nominal thicknesses as low as 10 nm vs. 15 nm for films grown in pure Ar discharges. In addition, *ex situ* analyses of discontinuous layer morphologies using scanning transmission electron microscopy (STEM), show that the origin of the flat morphology in nitrogen-modified growth is associated with the process of coalescence. Moreover, analyses of the film chemical composition reveal that the addition of N_2 in the sputtering atmosphere results in incorporation of 0.2 at.% N in the deposited layer. As far as EBE depositions are concerned, *in situ* and *ex situ* data show that, independently from the composition of the gas atmosphere, continuous layers are formed at nominal thicknesses of 25 nm and no N is detected in the deposited layer. Based on these findings, we argue that plasma-induced dissociation of molecular N_2 during sputtering creates atomic N that is adsorbed on the film growth front and delays island coalescence. This mechanism is not present in the case of EBE where the absence of plasma renders N_2 dissociation inactive.

The results presented herein underscore that accurate control of molecular gas dissociation rates is a key component for manipulating growth in weakly-interacting film-substrate systems using N_2 (and other polyatomic gases) as wetting agents. Moreover, attempts to further understand and model the effect of nitrogen on Ag-layer growth require considering the central role of atomic N species on various film formation stages.

2. Research methodology

2.1. Film synthesis

Ag films are synthesized by magnetron sputtering and electron-beam evaporation, without applying intentional heat to the substrate during deposition. Magnetron sputtering experiments are performed in a high-vacuum chamber at a base pressure of 10^{-5} Pa. The chamber is equipped with three confocally arranged magnetron sources, which form an angle of 25° with respect to the substrate normal and are positioned 180 mm away from the substrate surface. Vapor is generated by sputtering an elemental Ag target (diameter 76 mm; purity 99.99%; installed in one of the three magnetron sources) in either pure Ar or mixed Ar-N_2 atmosphere (N_2 partial pressure of 10% and, for selected samples used for chemical composition analysis, 25%) at a total pressure of 0.7 Pa (gas purity 99.999%). Depositions are performed in DCMS and HiPIMS modes by adjusting the time-averaged power in the range 26 to 34 W to achieve a film growth rate of 0.1 nm·s^{-1}, as determined by *ex situ* spectroscopic ellipsometry measurements (see Section 2C). For HiPIMS depositions, power is applied in the form of 50 μs long unipolar pulses with frequencies 200, 500, and 1000 Hz. Time-dependent target voltage and current waveforms during HiPIMS operation are recorded using a Picoscope® digital oscilloscope and show that the peak target power (P_{Tp}) increases from 0.7 to 4.1 kW as the pulsing frequency decreases from 1000 down to 200 Hz. This correlation between pulsing frequency and peak target power is a typical feature of the HiPIMS discharge [24], and it is leveraged herein to study the way by which plasma chemistry and energetics (as determined by P_{Tp}) affect film growth.

Czochralski-grown Si(0 0 1) wafers (with their 2 nm thick native SiO_x layer) are used as substrates with two different thicknesses: 100 μm for *in situ* wafer curvature measurements and 650 μm for *in situ* SDRS measurements (see Section 2B). To explore the universal character of our findings, films are deposited on two weakly-interacting surfaces: either directly on SiO_x/Si(0 0 1) substrates or on an 8 nm thick amorphous carbon (a-C) layer that is grown on the SiO_x/Si(0 0 1) substrate prior to the Ag-film deposition. For the synthesis of the a-C layer, a graphite target (installed in one of the two available magnetron sources in the deposition chamber; diameter 76 mm; purity 99.995 %) is sputtered in Ar atmosphere (working pressure of 0.3 Pa) by DCMS at a power of 180 W, yielding a growth rate of 0.016 nm·s^{-1}. Moreover, for selected experiments, electron-transparent carbon-coated copper grids are used as substrates, upon which STEM measurements are performed (see Section 2C).

EBE experiments are performed at high-vacuum conditions (base pressure 10^{-5} Pa) using an oblique angle of 11.2° with respect to the substrate normal, with the substrate-to-crucible distance being 450 mm. Films are grown on SiO_x/Si(0 0 1) substrates in pure N_2 and in pure Ar atmospheres (pressure 10^{-2} Pa), as well as without presence of any gas (pressure 10^{-5} Pa). The electron beam current is varied between 10 and 12 mA (at a constant voltage of 6.7 kV) to achieve a film growth rate of 0.1 nm·s^{-1}, as measured by a quartz crystal microbalance and confirmed by spectroscopic ellipsometry. The growth conditions for both sputtering and evaporation experiments are summarized in Table 1.

2.2. In situ growth monitoring

In the present work, we measure *in situ* the evolution of mechanical stresses and optical properties upon deposition for monitoring in real time film morphological evolution, from the initial growth stages to the formation of a continuous layer and beyond [25]. Stress is determined by measuring the substrate curvature change $\Delta\kappa$ using a magnification inferred curvature (MIC) setup [26] installed in the sputter-deposition chamber. The setup uses a light source to illuminate a plate, which features a 3×3 grid of holes, at an angle of incidence of 70° with respect to the substrate normal. A charge-coupled device camera collects the virtual image of the illuminated plate seen through the reflecting curved substrate acting as a spherical mirror, from which the curvature is determined. The product of stress (σ) and nominal film thickness (Θ) $\sigma \times \Theta$ is calculated from the expression [27],

$$\Delta(\sigma \times \Theta) = \frac{1}{6} Y_s h_s^2 \Delta\kappa$$

where $Y_s = 180.5$ GPa is the Si(1 0 0) substrate biaxial modulus and h_s is the substrate thickness.

Fig. 1(a) presents typical data in the form of $\sigma \times \Theta$ vs. Θ curves that are recorded during growth of Ag layers on a-C/SiO_x/Si substrates by DCMS in Ar (black solid line) and Ar-N_2 (blue dotted line) atmospheres. By convention, negative (positive) slope in a $\sigma \times \Theta$ vs. Θ curve corresponds to compressive (tensile) incremental stress. For growth in pure Ar, the incremental stress is initially compressive up to $\Theta \leq 2$ nm, followed by development of incremental tensile stress up to $\Theta \approx 14$ nm at which $\sigma \times \Theta$ reaches a maximum and a transition to incremental compressive stress occurs. The position of the tensile peak corresponds to the formation of a continuous film at a thickness $\Theta_{cont} = 13.9$ nm

Table 1
Summary of process conditions used for the synthesis of Ag films. Column 1 refers to the deposition method (DCMS – direct current magnetron sputtering; HiPIMS – high power impulse magnetron sputtering; EBE – electron-beam evaporation). Columns 2 and 3 list the time-averaged target power (P_{Tav}) and target voltage (V_T) used during DCMS and HiPIMS. Columns 4 and 5 list the pulsing frequency (f) and the resulting peak target power (P_{Tp}) during HiPIMS operation. Columns 6 through 8 refer to the composition of the growth atmosphere expressed as Ar and N_2 partial pressures (p_{Ar} and p_{N2}, respectively) and the ratio of p_{N2} to the total pressure during deposition ($\frac{p_{N2}}{p_{tot}}$). The synthesis conditions refer to films deposited on both a-C/SiO_x/Si and SiO_x/Si substrates.

Deposition method	P_{Tav}(W)	V_T(V)	f(Hz)	P_{Tp}(kW)	$\frac{p_{N2}}{p_{tot}}$	p_{N2}(Pa)	p_{Ar}(Pa)
DCMS	26	284	–	–	0	$< 10^{-5}$	7×10^{-1}
DCMS	26	290	–	–	0.1	7×10^{-2}	6.3×10^{-1}
HiPIMS	28	458	1000	0.7	0	$< 10^{-5}$	7×10^{-1}
HiPIMS	28	455	1000	0.7	0.1	7×10^{-2}	6.3×10^{-1}
HiPIMS	31	497	500	1.4	0.0	$< 10^{-5}$	7×10^{-1}
HiPIMS	31	506	500	1.5	0.1	7×10^{-2}	6.3×10^{-1}
HiPIMS	34	595	200	4.1	0	$< 10^{-5}$	7×10^{-1}
HiPIMS	34	603	200	4.0	0.1	7×10^{-2}	6.3×10^{-1}
EBE	–	–	–	–	–	10^{-2}	$< 10^{-5}$
EBE	–	–	–	–	–	$< 10^{-5}$	10^{-2}
EBE	–	–	–	–	–	$< 10^{-5}$	$< 10^{-5}$

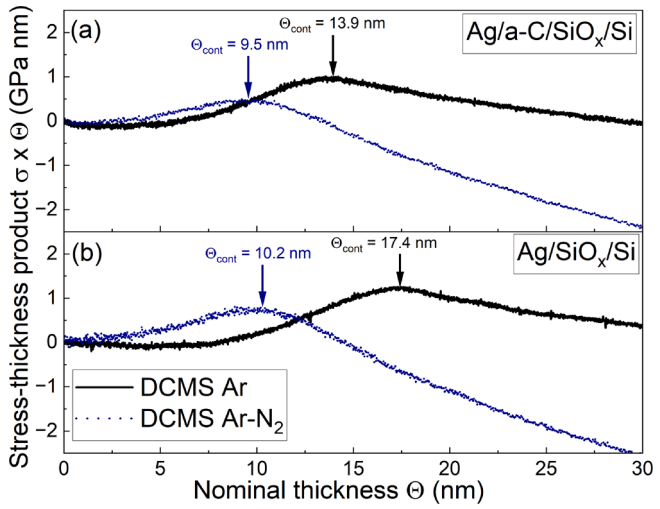

Fig. 1. Stress-nominal thickness ($\sigma \times \Theta$) vs. nominal thickness (Θ) curves recorded during the deposition of Ag by DCMS on (a) a-C/SiO_x/Si and (b) SiO_x/Si substrates in pure Ar (black solid lines) and mixed Ar-N_2 (blue dotted lines) atmospheres. The vertical arrows mark the position of the tensile-to-compressive stress transition which corresponds to the continuous formation thickness Θ_{cont} (Θ_{cont} value also provided in the figure). (For interpretation of the references to colour in this figure legend, the reader is referred to the web version of this article.)

(marked with a vertical arrow) [25,28]. Addition of N_2 to the plasmagenic Ar gas yields a $\sigma \times \Theta$ vs. Θ curve that exhibits a tensile incremental stress almost from the outset of the deposition, while the tensile-to-compressive transition occurs at a smaller nominal thickness corresponding to $\Theta_{cont} = 9.5$ nm. $\sigma \times \Theta$ vs. Θ curves recorded during Ag-layer growth on SiO_x/Si substrates (plotted in Fig. 1(b)) exhibit qualitatively similar trends to those obtained for growth on a-C/SiO_x/Si substrates, i.e., presence of N_2 in the sputtering atmosphere results in $\Theta_{cont} = 10.2$ nm, which is smaller than the value $\Theta_{cont} = 17.4$nm for deposition in pure Ar.

In situ monitoring of the Ag-layer optical response is carried out by real-time SDRS, using the setup described in Ref. [29]. The sample is illuminated with *p*-polarized white light emitted from a xenon arc lamp at an angle of 70° (DCMS and HiPIMS) or 60° (EBE) with respect to the surface normal. The reflected intensity is collected in the specular direction using an Ocean Optics QE65000 spectrometer within the spectral range $\lambda = 350 - 950$ nm. The relative variation of the sample reflectivity is measured during Ag deposition at a frequency of one spectrum per second as

$$\frac{\Delta R}{R_0}(\lambda, \Theta) = \frac{R(\lambda, \Theta) - R_0(\lambda)}{R_0(\lambda)} \quad (2)$$

where $R_0(\lambda)$ and $R(\lambda, \Theta)$ are the reflected intensities collected before the onset of Ag deposition and after depositing a Ag layer with a nominal thickness Θ, respectively. SDRS measurements are compared with modelled spectra that are calculated assuming that at each nominal thickness Θ the film fully wets the underlying substrate (i.e., exhibits an ideal 2D morphology) and grows at a constant deposition rate. The complex index of refraction required for calculating those spectra is either determined by *ex situ* spectroscopic ellipsometry (Ag and a-C; see Section 2C) or taken from Ref. [30] (Si).

Experimental and calculated SDRS data (solid blue and dashed black lines, respectively) corresponding to various nominal thicknesses Θ during growth of Ag on SiO_x/Si substrates by DCMS in pure Ar are shown in Fig. 2(a) ($\Theta = 2 - 10$ nm) and Fig. 2(b) ($\Theta = 12 - 30$ nm). During the early stages of deposition up to $\Theta = 8$ nm, the experimental spectra exhibit a broad peak that is associated with the excitation of localized surface plasmons, a consequence of 3D morphological evolution and formation of isolated Ag islands. The resonance frequency of the surface plasmon—corresponding to the wavelength λ_{max} at which $\frac{\Delta R}{R_0}$ exhibits its maximum—shifts continuously from $\lambda_{max} \approx 425$ nm at $\Theta = 2$ nm to $\lambda_{max} \approx 795$ nm at $\Theta = 8$ nm, indicating that the out-of-plane to in-plane aspect ratio of surface features (islands and/or clusters) and their interplanar (edge-to-edge) distance decrease with continued deposition. In addition, the calculated spectra show that $\frac{\Delta R}{R_0}$ increases monotonically as function of λ irrespective of the nominal thickness, while for the experimental $\frac{\Delta R}{R_0}$ spectra a negative slope (resulting from the surface-plasmon-induced maximum) is seen in the infrared wavelength range (700 –950 nm) for $\Theta \leq 8$ nm. Comparison between experimental and calculated spectra shows that they differ considerably for $\Theta < 12$ nm, while they are nearly identical for $\Theta \geq 15$ nm, i.e., a continuous Ag layer is formed for Θ in the range $12 - 15$ nm. The experimental and calculated $\frac{\Delta R}{R_0}$ spectra for Ag films deposited in Ar-N_2 atmosphere are plotted in Fig. 2(c) ($\Theta = 2 - 10$ nm) and Fig. 2(d) ($\Theta = 12 - 30$ nm). For those films, localized surface plasmons and a negative slope in the infrared range of the experimental $\frac{\Delta R}{R_0}$ data is only observed for spectra at $\Theta = 2$ nm and $\Theta = 4$ nm. Moreover, the calculated spectra match the experimental data for $\Theta \geq 10$ nm, i.e., addition of N_2 to the plasmagenic Ar gas results in the formation of a continuous layer at a smaller nominal thickness relative to growth in pure Ar, in qualitative agreement with the data presented in Fig. 1.

To quantify the differences established in Fig. 2(a)-(d), we plot in

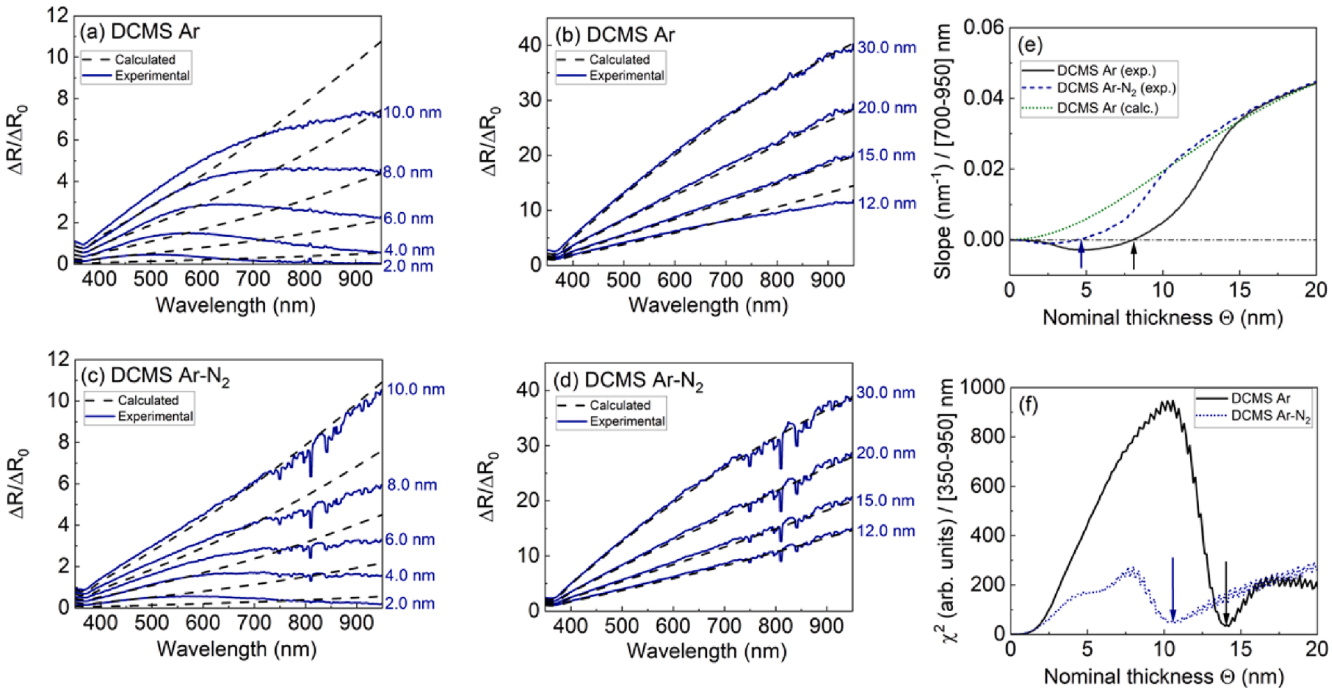

Fig. 2. (a)-(d) Experimental (blue solid lines) and calculated (black dashed lines) curves of differential reflectance $\frac{\Delta R}{R_0}$ of Ag layers deposited by DCMS on SiO_x/Si substrates at various nominal thicknesses Θ (Θ values are marked next to each spectrum) for growth in pure Ar (panels (a) and (b)) and in mixed Ar-N_2 (panels (c) and (d)) atmospheres. (e) Slope of $\frac{\Delta R}{R_0}$ spectra taken in the infrared range (700 −950nm) as a function of the nominal thickness Θ for growth in pure Ar (black solid line) and mixed Ar-N_2 (blue dashed line). The vertical arrows indicate the thickness at which the slope is zero, which corresponds to the percolation thickness Θ_{perc}. The green dotted line represents the calculated $\frac{\Delta R}{R_0}$ slope for growth by DCMS in pure Ar atmosphere (ideal 2D morphological evolution). (f) Mean square error χ^2 between experimental and calculated $\frac{\Delta R}{R_0}$ spectra (from panels(a)-(d)) as a function of the nominal thickness Θ (black solid and blue dashed lines correspond to spectra recorded during growth in Ar and Ar-N_2, respectively). The vertical arrows indicate the nominal thickness at which χ^2 exhibits a local minimum and corresponds to the continuous film formation thickness Θ_{cont}. (For interpretation of the references to colour in this figure legend, the reader is referred to the web version of this article.)

Fig. 2(e) the slope of the experimental $\frac{\Delta R}{R_0}$ curves taken in the infrared region as a function of Θ for the set of data corresponding to growth in Ar (black solid line) and Ar-N_2 (blue dashed line) atmosphere. The curve corresponding to the slope of calculated $\frac{\Delta R}{R_0}$ data (Ar atmosphere) assuming ideal 2D morphological evolution is also plotted for reference (dotted green line). The point at which the experimental slope reaches zero (marked with vertical arrows) serves as an upper limit for the percolation threshold thickness Θ_{perc} (i.e., the thickness at which the film electrically conducts over macroscopic distances, though not being yet continuous) [28]. We see that $\Theta_{perc} = 8$ nm for growth in pure Ar, while addition of N_2 to the gas atmosphere yields earlier percolation at $\Theta_{perc} = 4.5$ nm. For determining Θ_{cont}, we evaluate the evolution of the mean square error χ^2 between experimental and calculated $\frac{\Delta R}{R_0}$ spectra. The χ^2 vs. Θ curves corresponding to Ar and Ar-N_2 grown Ag films are plotted in Fig. 2(f) (black solid and blue dashed line, respectively). The local minimum of χ^2 corresponds to Θ_{cont} [28] (position marked with vertical arrow in the corresponding curve) and decreases from $\Theta_{cont} = 14.2$ nm to $\Theta_{cont} = 10.7$ nm upon addition of N_2 to the Ar sputtering atmosphere. In the remainder of the article, the values of Θ_{cont} and Θ_{perc} determined by $\sigma \times \Theta$ vs. Θ curves and $\frac{\Delta R}{R_0}$ spectra, are used as proxies for assessing the 3D/2D character of film growth for the various process conditions, whereby decrease of Θ_{cont} and Θ_{perc} is consistent with formation of films with flatter morphology, as evidenced by x-ray reflectometry and atomic-force microscopy data in previous studies [19,31].

2.3. Ex situ characterization

Film morphologies of discontinuous layers during the initial stages of Ag growth are studied by means of high-angle annular dark-field (HAADF) STEM. Experiments are conducted using a Thermo Scientific Talos F200S transmission electron microscope, which is operated at an acceleration voltage of 200 kV, with a semi-convergence angle of 10.5 mrad for an average probe current (size) of 30 pA (0.16 nm). Plan-view HAADF-STEM images are recorded for Ag films (nominal thicknesses ranging from 0.3 to 6 nm; synthesis conditions selected from those listed in Table 1) deposited on electron-transparent carbon-coated copper grids, which are overcoated with an 8 nm thick a-C layer grown at the conditions detailed in Section 2A. The same 8 nm thick a-C film is also deployed immediately after Ag growth as a capping layer to minimize post-growth morphological changes when the sample is exposed to: (i) the atmosphere during transfer from the synthesis chamber to the microscope; and (ii) the electron beam during the HAADF-STEM experiments. The ImageJ software [32] is used to binarize the pixel intensities of the recorded images so that intensities representing film and substrate become one and zero, respectively. The threshold for the binarization is set through the default procedure of ImageJ which is based on the isodata algorithm [33]. The binarized images are then analyzed to compute the fraction of the substrate area Q covered by the deposited Ag film, the number density N_i of objects (i.e., islands and/or clusters) on the film surface, the object size D (D is the diameter of a disk having the same projected area as that of a given object), and the object in-plane aspect ratio AR (for the latter, the objects are approximated by ellipses and AR is the ratio of the minor-to-major ellipse axis).

Besides morphology of discontinuous layers, we also study the crystal structure of continuous films by means of x-ray diffractometry (XRD). XRD measurements are performed on 35 nm thick Ag layers grown on SiO_x/Si substrates using a Seifert XRD 3000 four-circle diffractometer with point focus geometry, Cu Kα wavelength (1.5418 Å), and a Meteor0D detector. θ −2θ scans are acquired in Bragg-Brentano configuration over the 2θ angular range 32 −50°, which includes both the 111 and 200 Ag reflections.

Spectroscopic ellipsometry is employed to determine the optical properties and thickness of Ag films deposited on SiO_x/Si and a-C/SiO_x/Si substrates, as well as the optical properties of the a-C layer deposited on SiO_x/Si. Ellipsometric angles Ψ and Δ are recorded at three angles of incidence (65°, 70°, and 75° measured from the substrate normal) in the spectral range 200 − 1700 nm, using a Woolam M2000UI instrument. A three-phase model consisting of substrate, film, and vacuum is fitted to the acquired data. The substrate is modelled as a 650 μm semi-infinite Si slab, the optical properties of which are taken from Ref. [30]. The optical response of the Ag film is described by the Drude free-electron model, while the a-C layer is fitted with a Lorentz oscillator [34]. The obtained layer optical constants (i.e., complex index of refraction) are used for computing the calculated SDRS curves in Fig. 2.

Global elemental composition and concentration depth profiles of the films are determined by time-of-flight elastic recoil detection analysis (ToF-ERDA) in the EGP-10-II 5MV tandem accelerator of the Helsinki Accelerator Laboratory [35]. Measurements are performed using a 40 MeV ^{127}I ion beam, with the detector positioned at an angle of 40° with respect to the direction of the incident beam, while the beam incident direction forms an angle of 20° with respect to the sample surface. Composition and depth profiles are calculated using stopping forces obtained from the SRIM freeware [36], the measurement geometry, and Rutherford elastic recoil cross sections for the detected elements.

ToF-ERDA measurements are complemented by x-ray photoelectron spectroscopy (XPS) analyses. Measurements are performed in an XPS instrument from Hiden Analytical Ltd. Photoelectron spectra are acquired by using an Argus photoelectron energy analyzer (Omicron NanoTechnology GmbH) and a standard Mg source (Kα line, photon energy of 1253.6 eV; pass energy 20 eV). Binding energies are referenced to C1s peak of ambient hydrocarbons at 284.8 eV. The CasaXPS software package is used for peak fitting and data analysis.

3. Results and discussion

3.1. Morphological evolution of percolated and continuous films

Fig. 3 plots the continuous formation thickness Θ_{cont} of Ag films grown on SiO_x/Si substrates by DCMS, HiPIMS (pulsing frequencies 200 and 1000 Hz), and EBE. Hollow symbols represent Θ_{cont} values determined by *in situ* SDRS, whereby black squares and blue circles correspond to samples grown in pure Ar and mixed Ar-N_2 (or pure N_2 for EBE) atmospheres, respectively. Moreover, the black diamond symbol is the Θ_{cont} value of the EBE sample grown without the presence of any gas. The data show that growth in pure Ar using sputtering-based techniques (DCMS and HiPIMS) yields Θ_{cont} with values in the range 14.2 to 15.1 nm. Addition of N_2 to the sputtering atmosphere results in lower Θ_{cont} (values range from 10.5 to 11.1 nm), i.e., 2D morphological evolution is promoted in agreement with previous observations [17,19]. Concurrently, growth by EBE (at all gas atmospheres used) yields values for Θ_{cont} from 23.9 to 27.3 nm. However, the differences are within the error bars of the respective data points, i.e., the presence of N_2 during EBE growth of Ag on SiO_x/Si substrates has no statistically significant effect on the film morphological evolution. For reference, Θ_{cont} determined from wafer curvature measurements using the MIC setup are also plotted (filled symbols) for samples grown by DCMS. The MIC-based analysis shows qualitatively similar trends to those obtained from SDRS data, i.e., presence of N_2 leads to a $\Theta_{cont} = 10.2$ nm vs. $\Theta_{cont} = 17.4$ nm for growth in pure Ar. We attribute the difference between SDRS- and MIC-determined Θ_{cont} for samples grown by DCMS in pure Ar to random variations in the surface roughness and composition of the native SiO_x layer among different substrates upon which Ag is deposited. This notwithstanding, both SDRS and wafer curvature measurements confirm that addition of N_2 to the sputtering atmosphere favors an earlier continuous film formation.

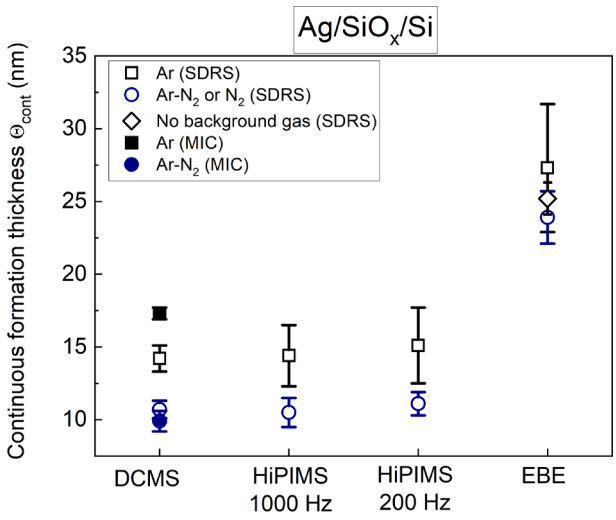

Fig. 3. Continuous film formation thickness Θ_{cont} of Ag films grown on SiO_x/Si substrates by DCMS, HiPIMS (pulsing frequencies 200 and 1000Hz), and EBE. Squares and circles correspond to data from samples grown in pure Ar and mixed Ar-N_2 (or pure N_2 for EBE samples) atmospheres, respectively. The diamond symbol is the Θ_{cont} value for the sample grown by EBE without presence on any gas. Hollow and filled symbols represent Θ_{cont} values extracted from in situ SDRS and wafer curvature measurements, respectively. For SDRS data, error bars are estimated from the width of the minimum in the χ^2 vs Θ curves (see Fig. 2(f)). For MIC data, error bars correspond to width of the plateau of the maximum in the $\sigma \times \Theta$ vs. Θ curves (see Fig. 1) that delineates the tensile-to-compressive incremental stress transition.

To ascertain whether the trends pertaining to the 2D/3D character of continuous-layer growth (established in Fig. 3) also hold for earlier film-formation stages, we plot in Fig. 4 the percolation thickness Θ_{perc} (determined by *in situ* SDRS) of Ag films deposited on SiO_x/Si substrates by DCMS, HiPIMS (pulsing frequencies 200 and 1000 Hz), and EBE. Black squares and blue circles correspond to samples grown in pure Ar

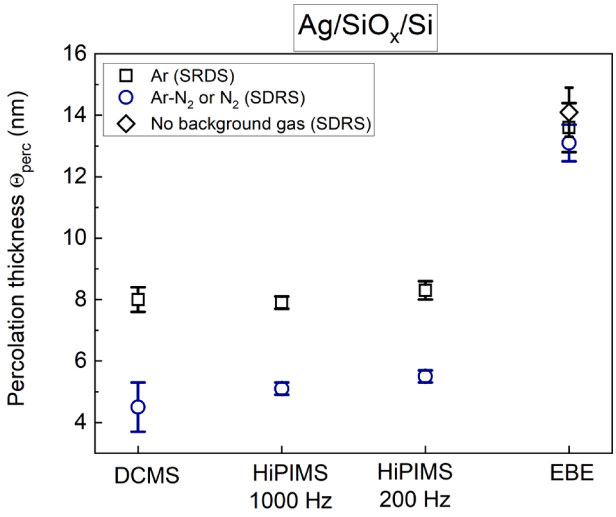

Fig. 4. Percolation thickness Θ_{perc} (determined by in situ SDRS measurements) of Ag films grown on SiO_x/Si substrates by DCMS, HiPIMS (pulsing frequencies 200 and 1000Hz), and EBE. Squares and circles correspond to data from samples grown in pure Ar and mixed Ar-N_2 (or pure N_2 for EBE samples) atmospheres, respectively. The diamond symbol is the Θ_{perc} value for the sample grown byy EBE without presence on any gas. Error bars are estimated based on the nominal thickness values at which the experimental $\frac{\Delta R}{R_0}$ slope measured in different spectral ranges (700 −850nm and 800 −950nm) becomes positive as depicted in Fig. 2(e) and explained in Section 2B.

and mixed Ar-N_2 (or pure N_2 for EBE) atmospheres, respectively, while the black diamond shows the Θ_{cont} value of the EBE sample grown without the presence of any gas. We see that growth of Ag by sputtering (both DCMS and HiPIMS) in pure Ar yields Θ_{perc} values from 7.9 to 8.3 nm, which decrease down to 4.5 – 5.5 nm upon N_2 addition. In contrast, the composition of the gas atmosphere has no effect for EBE, since at all deposition conditions the mean Θ_{perc} values range from 13.1 to 14.1 nm and exhibit overlapping error bars. Thus, we establish that the effect of the plasmagenic gas composition on Θ_{perc} is in qualitative agreement with that on Θ_{cont}, i.e., N_2 promotes 2D morphology of continuous layers by affecting growth stages before the formation of a percolated network. This is consistent with the notion that the overall film morphological evolution is primarily the result of dynamic competition between island growth and coalescence during the incipient film-formation stages [37–39]. Moreover, we see that the ratio $\frac{\Theta_{cont}}{\Theta_{perc}} \approx 2$ is in agreement with previous works of ours [31,40,41].

To explore the universal character of the trends seen in Figs. 3 and 4, we plot in Fig. 5 the continuous formation thickness Θ_{cont} (determined by *in situ* wafer curvature measurements) of Ag films, grown on a-C/SiO_x/Si substrates by DCMS and HiPIMS (pulsing frequencies 200, 500, 1000 Hz), in Ar (black squares) and Ar-N_2 (blue circles) atmospheres. The results are in qualitative agreement with those obtained for growth on SiO_x/Si, i.e., N_2 promotes 2D morphological evolution as manifested by the decrease of Θ_{cont} values from the range 13.8 – 15.3 nm (Ar) to 9.5 – 11.5 nm (Ar-N_2). We note that in Fig. 5 we only report data from MIC analysis. The reason is that the use of the SDRS-based methodology may be restricted by the dielectric characteristics of the material upon which Ag growth proceeds: while SiO_x possesses good insulating properties and hence yields a pronounced surface plasmon resonance, the higher conductivity of a-C results in damping of the surface plasmon resonances and of the features in the $\frac{\Delta R}{R_0}$ slope and χ^2 vs. Θ curves, rendering the determination of Θ_{perc} and Θ_{cont} ambiguous.

3.2. Morphology of discontinuous layers and film crystal structure

To correlate the trends with respect to Θ_{perc} and Θ_{cont} observed in Figs. 3-5 with the initial stages of island nucleation, growth, and coalescence, we perform plan-view HAADF-STEM imaging of a-C/Ag/a-C films deposited on electron-transparent carbon-coated copper grids. Ag films are synthesized by DCMS (in Ar and in Ar-N_2 atmospheres) and HiPIMS (pulsing frequency 1000 Hz in Ar-N_2 atmosphere) at nominal thicknesses Θ of 0.3, 0.6, 3.0 nm, and 6.0 nm. The micrographs are presented in Fig. 6(a) and reveal that the overall morphological evolution as a function of Θ is independent from the composition of the sputtering atmosphere and the choice of the deposition method: nearly spheroidal nanoscale islands at $\Theta = 0.3$ nm increase in size at $\Theta = 0.6$ nm, primarily due to attachment of newly deposited atoms. Further deposition renders island impingement and coalescence the dominant structure-forming processes, manifesting itself by a notable decrease in the object density ($\Theta = 3.0$ nm). Moreover, the micrographs at $\Theta = 3.0$ nm feature both seemingly spheroidal islands and clearly elongated structures, which indicates that the coalescence becomes partially incomplete as the growth rate of the islands in coalescing clusters exceeds the rate of cluster reshaping. This surface configuration serves as the precursor for the morphology to evolve into an interconnected network of elongated clusters as the nominal thickness increases to $\Theta = 6.0$ nm.

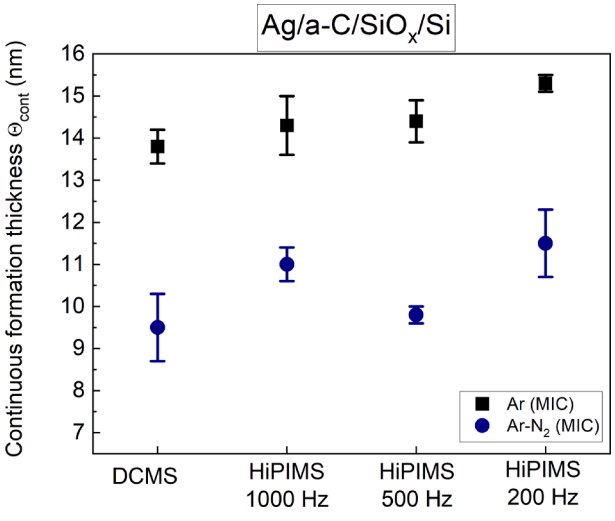

Fig. 5. Continuous film formation thickness Θ_{cont} (determined by in situ wafer curvature measurements) of Ag films grown on a-C/SiO_x/Si substrates by DCMS and HiPIMS (pulsing frequencies 200, 500, 1000 Hz). Squares and circles correspond to data from samples grown in pure Ar and mixed Ar-N_2 atmospheres, respectively. Error bars correspond to width of the plateau of the maximum in the $\sigma \times \Theta$ vs. Θ curves (see Fig. 1) that delineates the tensile-to-compressive incremental stress transition.

The results of the quantitative analyses of the micrographs in Fig. 6 (a) with respect to the density N_i, the size D, and the aspect ratio AR of the objects imaged on the substrate surface are summarized in Table 2. At all deposition conditions, the island density N_i exhibits values in the range 4.0×10^{12} to 4.9×10^{12} cm^{-2} for $\Theta = 0.3$ nm. Such variation in N_i (20%) is rather marginal [11,42] and it implies that the composition of the gas atmosphere and the choice of the deposition method does not significantly affect the dynamic competition between island nucleation and growth that determines the magnitude of island density. Increase of Θ to 0.6 nm leads to $N_i = 2.7 - 2.8 \times 10^{12}$ cm^{-2}, which further decreases to $3.0 - 4.0 \times 10^{11}$ cm^{-2} for $\Theta = 3.0$ nm.

The distributions of object size D for the micrographs corresponding to $\Theta = 0.3$, 0.6 and 3.0 nm in Fig. 6(a), are presented in Fig. S1 in the supporting information file [43]. From the distributions in Fig. S1, we determine the mean value $\overline{D}$ and its standard deviation σ_D, which we list as $\overline{D} \pm \sigma_D$ in Table 2. For $\Theta = 0.3$ nm, and irrespective of deposition conditions, the mean island sizes are 2 nm. Upon increasing Θ to 0.6 nm, $\overline{D}$ increases to 3 nm, while the distributions become broader (manifested by an increase of the standard deviation σ_D) most notably for films grown in Ar-N_2 gas atmospheres. Further increase of Θ to 3.0 nm yields an object size of 11.5 nm for the sample grown by DCMS in Ar atmosphere, while addition of N_2 to the plasmagenic gas (both for DCMS and HiPIMS) results in $\overline{D} \approx 14$ nm. The latter is consistent with a more interconnected cluster morphology compared to the one obtained for growth in pure Ar atmosphere.

The object aspect ratio AR distributions for nominal thicknesses of 0.3, 0.6, and 3.0 nm are plotted in Fig. S2 [43] and the corresponding $\overline{AR} \pm \sigma_{AR}$ values are presented in Table 2. Upon increasing Θ from 0.3 to 3.0 nm, $\overline{AR}$ decreases from 0.85 to 0.7 and the respective distributions become progressively broader, i.e., the objects on the substrate surface become more elongated. Moreover, the $\overline{AR}$ values for $\Theta = 3.0$ nm are somewhat smaller (i.e., clusters are more elongated) for samples grown in mixed Ar-N_2 ambient, as compared to samples deposited in pure Ar.

The interconnected network of elongated clusters observed for $\Theta = 6.0$ nm does not allow us to accurately determine the object density, size, and aspect ratio. However, it is clearly visible that the areal coverages Q of the samples grown by DCMS and HiPIMS in Ar-N_2 atmosphere are larger as compared to that of the samples grown in pure Ar. The evolution of Q vs. nominal thickness Θ is plotted in Fig. 6(b). There it is seen that samples grown in Ar-N_2 mixtures exhibit similar areal coverage values (green circles and blue triangles for DCMS and HiPIMS, respectively), while the corresponding areal coverage values for samples grown by DCMS in pure Ar (black squares) are smaller for $\Theta \geq 3.0$ nm. The results presented in Fig. 6 are consistent with the data in Figs. 3 -5, i.e., presence of N_2 in the sputtering atmosphere favors 2D morphological evolution and thereby formation of a continuous layer at smaller nominal thicknesses as compared to samples grown in pure Ar. Moreover, the

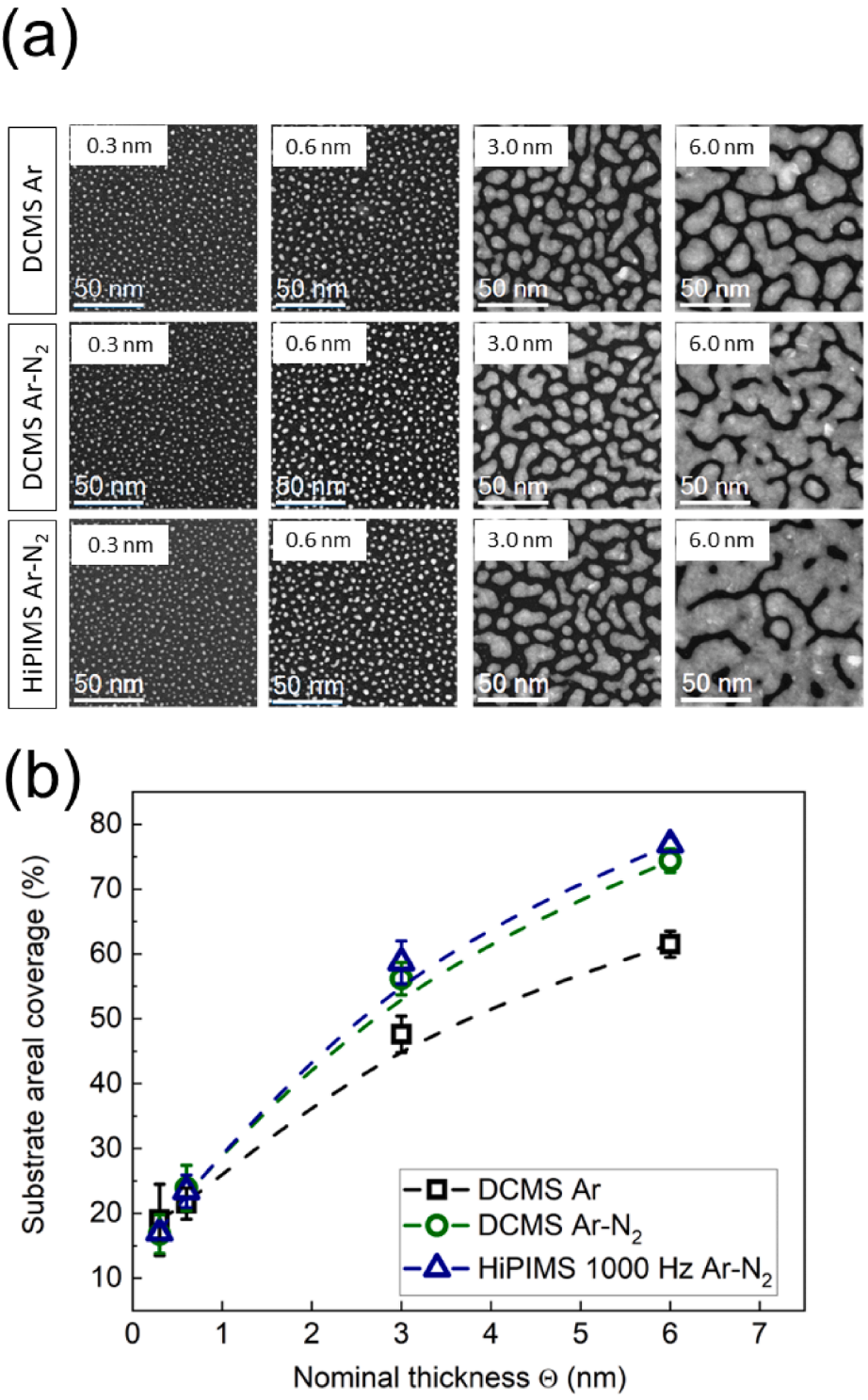

Fig. 6. (a) Plan-view HAADF-STEM micrographs of Ag films grown on electron-transparent carbon-coated copper grids. Before Ag growth, the carbon-coated grids are covered by an 8 nm thick a-C layer, while immediately after Ag growth the deposited film is capped by a 8 nm a-C layer to minimize post-growth morphological changes upon exposure of the sample to the atmosphere and the electron beam during the STEM observation. The micrographs are collected from films of various nominal thicknesses (as indicated in the micrographs) grown by DCMS in pure Ar atmosphere (top row), DCMS in mixed Ar-N_2 atmosphere (middle row), and HiPIMS at a pulsing frequency of 1000 Hz in mixed Ar-N_2 atmosphere (bottom row). (b) Substrate areal coverage vs nominal thickness extracted by analyzing HAADF-STEM micrographs at the synthesis conditions shown in the top panel. The error bars are determined by measuring the surface area with a contrast threshold of ±5% with respect to the default threshold, which is set according to the procedure described in Ref[33]. The dashed lines are guides to the eye.

fact that differences in areal coverage, island size distribution, and island shape are observed for $\Theta \geq 3.0$ nm means that N_2 promotes 2D morphology by delaying the process of island reshaping during coalescence, such that coalescing clusters exhibit a larger in-plane expansion rate vs. out-of-plane growth. This in in agreement with previous studies pertaining to the role of N_2 [8,17,19], O_2 [20,21], and other metals [15] as surfactants during Ag-layer growth on weakly-interacting substrates.

Plan view HAADF-STEM data and analyses are complemented by

Table 2
Results of quantitative analyses of plan-view micrographs from Fig. 6(a). Columns 4, 5, and 6 list the density N_i, size D, and in-plane aspect ratio AR, respectively, of the objects imaged on the substrate surface. For D and AR the mean value ± standard deviation ($\overline{D} \pm \sigma_D$ and $\overline{AR} \pm \sigma_{AR}$) is listed, both determined the size and aspect ratio distributions shown in Figs. S1 and S2, respectively.

Deposition method	Gas atmosphere	Nominal thickness Θ (nm)	Density N_i (cm^{-2})	Size D (nm)	Aspect ratio AR
DCMS	Ar	0.3	4.5×10^{12}	2.21 ± 0.73	0.86 ± 0.06
DCMS	Ar	0.6	2.8×10^{12}	2.95 ± 0.96	0.76 ± 0.11
DCMS	Ar	3.0	4.0×10^{11}	11.6 ± 3.20	0.73 ± 0.15
DCMS	Ar-N_2	0.3	4.0×10^{12}	2.20 ± 0.70	0.84 ± 0.06
DCMS	Ar-N_2	0.6	2.7×10^{12}	3.20 ± 0.94	0.70 ± 0.11
DCMS	Ar-N_2	3.0	3.0×10^{11}	14.1 ± 4.87	0.68 ± 0.19
HiPIMS	Ar-N_2	0.3	4.9×10^{12}	1.98 ± 0.68	0.86 ± 0.06
HiPIMS	Ar-N_2	0.6	2.7×10^{12}	3.22 ± 1.13	0.79 ± 0.07
HiPIMS	Ar-N_2	3.0	3.0×10^{11}	14.1 ± 4.64	0.71 ± 0.18

XRD measurements on continuous (35 nm thick) films grown by DCMS and HiPIMS (1000 Hz) in Ar and Ar-N_2 atmospheres, as well as by EBE in the absence of any gas and in pure N_2 atmosphere. Both 111 and 200 reflections are detected in the XRD patterns of all samples, as seen in Fig. S3 in the supporting information file [43]. The 111 reflections are dominant for films grown in Ar atmosphere (DCMS, HIPIMS) or in the absence of any gas (EBE), i.e., those films exhibit a pronounced < 111 > crystallographic texture. Addition of N_2 to the plasmagenic gas leads to an increase of the intensity of the 200 reflections (relative to that of 111 reflections) for films grown by DCMS and HiPIMS. Concurrently, all XRD reflections become broader (the full width at half maximum increases to 0.5° vs. 0.4° for growth in pure Ar atmosphere) indicating a decrease in crystallite size. Given that coalescence completion is a key process for texture selection and grain coarsening [44], the XRD data for DCMS- and HiPIMS-grown films are consistent with the notion that N_2 addition to the plasmagenic gas leads to an earlier onset of incomplete coalescence. In contrast to the films synthesized by magnetron sputtering, the XRD pattern of EBE-grown films is not affected by the N_2 addition to the deposition atmosphere, which is consistent with the results presented in Figs. 3 and 4.

3.3. Chemical composition and bonding properties

Compositional analysis by means of ToF-ERDA shows that all samples predominantly consist of Ag (content > 99 at. %) and contain small fractions of impurities, including hydrogen, carbon, and nitrogen (N). In particular, we find that films grown by sputtering (both DCMS and HiPIMS) in mixed Ar-N_2 ambient ($\frac{p_{N2}}{p_{tot}} = 0.1$) exhibit a N content in the range 0.1 −0.2 at. %, while for samples grown in pure Ar the N content is < 0.05 at. %, i.e., below the ToF-ERDA detection limit. The latter is also the case for samples synthesized by EBE, irrespective of the composition of the gas atmosphere. Since the N content of 0.1 −0.2 at. % is rather low and close to the detection limit of ToF-ERDA, we also grow a reference 200 nm thick Ar-N_2 DCMS sample (on SiO_x/Si substrate) at $\frac{p_{N2}}{p_{tot}} = 0.25$ to ascertain the ability of the technique to measure small variations in light elements content. The analysis shows that increase of $\frac{p_{N2}}{p_{tot}}$ to 0.25 leads to a clear increase of the N content to 0.3 at. % vs. 0.17 at. % for a 200 nm thick reference sample grown at $\frac{p_{N2}}{p_{tot}} = 0.1$. Moreover, N is present throughout the film thickness as seen in the depth profile data shown in Fig. S4 [43].

ToF-ERDA measurements are complemented by XPS analyses of Ag films grown on a-C/SiO_x/Si substrates by DCMS in pure Ar and mixed Ar-N_2 atmospheres. Survey XPS scans (not shown here) reveal the existence of all Ag-related peaks (Ag-3 s, Ag-3p, Ag-3d, Ag-4 s, and Ag-4p). In addition, high resolution core-level Ag-3d scans (plotted in Fig. S5 [43]) show that only Ag-Ag bonds are detected in the films, even for synthesis conditions at which ToF-ERDA measurements show N incorporation in the Ag layer. This may be explained by the relatively small N content (0.17 at. %), but it is also consistent with previous studies which report that no Ag-N compounds form during sputter deposition in N_2-containing gas atmospheres [8,17,19,45]. Such lack of compound formation may also lead to a relatively easy desorption of N from the growing surface, which can be the reason for which only trace amounts of N are found even though the gas atmospheres contain N_2 with partial pressures as high as 25 %. High resolution N1s scans (not presented here) are consistent with the notion of N incorporation in the films. However, the signal is dominated by surface contamination, hence quantification of the N content by XPS is not possible.

3.4. Structure-forming mechanisms and growth dynamics

In Figs. 3 and 4, we see that Θ_{perc} and Θ_{cont} values for EBE-deposited films are clearly larger than those of their sputtered-deposited (both DCMS and HiPIMS) counterparts, i.e., EBE yields a more pronounced 3D morphological evolution. The 2D/3D character of film growth, as reflected in the magnitude of Θ_{perc} and Θ_{cont}, is determined by the dynamic competition between island growth and island coalescence completion rate. For a given nominal thickness, the former increases with increasing the vapor arrival (i.e., deposition rate) on the growing film surface until the point that the time required for neighboring islands to impinge upon another becomes equal to the time required for a coalescing cluster to reshape and relax to its equilibrium shape [37,39–41,46]. Beyond that point, coalescence becomes incomplete and an interconnected network of elongated clusters forms leading to a percolated and eventually a continuous layer. Since both EBE and sputtering experiments are conducted at identical deposition (i.e., vapor arrival) rates of $0.1\ nm \cdot s^{-1}$, the differences in Θ_{cont} and Θ_{perc} seen in Figs. 3 and 4 cannot be attributed to the process of island growth and impingement. The key difference between EBE and sputtering is that in the latter technique the growing surface is exposed to bombardment by hyperthermal gas and metal species with energies of a few eV to a few tens of eV. Such bombardment may either enhance island nucleation density via cluster dissociation and surface defect formation or it may decrease nucleation probability on terraces due to enhancement of adatom mobility [11,47,48]. Both scenarios can potentially promote 2D morphological evolution since: (i) a higher density and thereby smaller size of 3D nuclei on the substrate surface would result in a higher in-plane substrate surface coverage during the initial film growth stages; and (ii) a decreased layer nucleation rate on flat sidewall facets of nanoscale islands would hinder facet migration across islands and mass transport during island coalescence and cluster reshaping, thereby leading to an earlier onset of elongation and percolation transition [49].

An additional feature of the sputtering processes is that interactions of energetic plasma electrons with gas species can modify the plasma chemistry. In the case of Ar-N_2 gas mixtures used in the present study, energetic electrons may dissociate molecular N_2 into atomic N [22,23]. Yun *et al.* [17] have suggested that atomic N generated in sputtering discharges acts as surfactant that reduces the surface free energy of nanoscale Ag islands and improve their wetting on weakly-interacting ZnO substrates. This effect can be considered equivalent to N species

delaying the 3D reshaping of islands during coalescence and thereby promoting 2D morphological evolution for sputtered Ag films grown on SiO_x/Si and a-C/SiO_x/Si in the present study.

Gervilla *et al.* [49] have suggested that coalescence of faceted nanoscale islands during film growth occurs by migration of sidewall facet layers from one island of the coalescing cluster to the other, such that one island is effectively absorbed by the other. This process is mediated by a net flux of atoms via the intersection formed at the neck area of the coalescing cluster, followed by nucleation and growth of sidewall facet layers. Adsorption of N on the island facets may disturb the net atomic flux and thereby delay the facet-layer migration across islands. Dedicated studies enabling to image and obtain atomic-scale compositional information from coalescing clusters, along with growth simulations will be required to shed further light on atomistic processes that govern morphological evolution of Ag films under the presence of N and other surfactant species. We also note that the effect of N on film morphology is associated with incorporation of trace amounts of N (0.2 at. %) in the Ag layers as shown in Section 3C. This does not rule out that significantly larger coverages of N are established on the film surface during growth. Given that no Ag-N compounds form, it is likely that atomic N floats on the film surface (i.e., acts a surfactant) and eventually undergoes associative desorption in the form of N_2 [50].

The absence of plasma in EBE yields a gas atmosphere that only contains molecular N_2. Such molecular species are expected to have significantly shorter residence times on the film surface (as compared to the more active atomic N species) [50,51] and hence they have no effect on film growth. When comparing DCMS to HiPIMS, one should expect that the higher electron density in HiPIMS would result in higher N_2 dissociation rates and thereby a more pronounced effect on film morphological evolution. This effect is not observed in our data, and it might indicate that the plasma conditions, in terms of peak power used in our experiments, are not sufficient to yield a noticeable difference in plasma chemistry, considering the relatively large N_2 dissociation energy of 9.8 eV [22]. An alternative explanation is that the N flux generated by N_2 dissociation during DCMS is sufficient to adsorb on available Ag surface sites, such that an increase of N atom supply when using HiPIMS has no effect on the film growth evolution. The overall findings with respect to EBE-, DCMS-, and HiPIMS-grown films call for investigations in which plasma chemistry and energetics are systematically and independently varied (e.g., by using external ion sources for generating N beams of well-defined energy) for further understanding the effect of N_2 on the morphological evolution of Ag films on weakly-interacting substrates.

4. Summary and conclusions

In the present work, we study the effect of N_2 gas on the vapor-based growth of thin Ag films on weakly-interacting amorphous carbon (a-C) and SiO_x surfaces. To access a wide range of conditions with respect to energies and ionization degrees of film-forming and plasma species, as well as the propensity towards atomic N generation via N_2 dissociation, film deposition is carried out by three methods, i.e., direct current magnetron sputtering (DCMS), high-power impulse magnetron sputtering (HiPIMS), and electron-beam evaporation (EBE). Using *in situ* and real-time substrate curvature measurements and surface differential reflectance spectroscopy, we find that addition of N_2 to DCMS and HiPIMS discharges promotes formation of continuous layers at nominal thicknesses of 10 nm, considerably smaller compared to that for films grown in pure Ar atmosphere (15 nm). *In situ* analyses are combined with *ex situ* transmission electron microscopy studies of discontinuous layer morphologies which reveal that the origin of 2D morphology in nitrogen-modified growth is caused by delay of island reshaping during the process of coalescence. Moreover, ion beam-based composition analysis reveals that N_2 in the sputtering atmosphere results in an incorporation of 0.1 −0.2 at.% N in the deposited layer. Concurrently, no effect on film morphology and composition is observed when N_2 is present in the growth atmosphere during EBE depositions. Based on these findings, we argue that plasma-induced dissociation of molecular N_2 during sputtering causes prolonged adsorption of atomic N onto the film growth front thereby delaying island coalescence, while the absence of plasma and hence dissociation during EBE renders N_2 ineffective for affecting film growth. The results presented herein show that further manipulation and optimization of Ag and metal film morphology on weakly-interacting substrates using gaseous species as surfactants requires accurate control of the plasma chemistry in terms of dissociation of molecular species to their atomic constituents, as well as deeper understanding of the plasma chemistry on the dynamics of the various film-forming processes.

CRediT authorship contribution statement

K. Sarakinos: Conceptualization, Formal analysis, Funding acquisition, Investigation, Methodology, Writing – original draft, Writing – review & editing, Resources. **D. Babonneau:** Conceptualization, Formal analysis, Funding acquisition, Investigation, Methodology, Resources, Writing – review & editing. **J. Ramade:** Formal analysis, Investigation, Writing – review & editing. **Y. Robin:** Methodology, Writing – review & editing. **K. Solanki:** Investigation. **K. Mizohata:** Formal analysis, Investigation, Writing – review & editing. **V. Tuboltsev:** Investigation, Writing – review & editing. **N. Pliatsikas:** Formal analysis, Writing – review & editing. **B. Krause:** Formal analysis, Funding acquisition, Writing – review & editing. **G. Abadias:** Conceptualization, Formal analysis, Funding acquisition, Investigation, Resources, Writing – review & editing.

Declaration of Competing Interest

The authors declare that they have no known competing financial interests or personal relationships that could have appeared to influence the work reported in this paper.

Data availability

Data will be made available on request.

Acknowledgements

K.S. acknowledges financial support from the Swedish Research Council (Grant No. VR-2021-04113), the Åforsk foundation (Grant No. 22-150), and the University of Poitiers, France, for granting a visiting professorship in the period June-July 2022. This work is part of the IRMA project funded by the French National Research Agency (ANR) and the German Research Foundation (DFG) through the respective grants ANR-21-CE09-0041-01 and DFG-491224986. The work also pertains to the French Government programs “Invertissements d’Avenir” (EUR INTREE, reference ANR-18-EURE-0010) and LABEX INTERACTIFS (reference ANR-11-LABX-0017-01).

Appendix A. Supplementary data

Supplementary data to this article can be found online at https://doi.org/10.1016/j.apsusc.2023.159209.

References

[1] X. Liu, Y. Han, J.W. Evans, A.K. Engstfeld, R.J. Behm, M.C. Tringides, M. Hupalo, H.-Q. Lin, L. Huang, K.-M. Ho, D. Appy, P.A. Thiel, C.-Z. Wang, Growth morphology and properties of metals on graphene, Prog. Surf. Sci. 90 (2015) 397–443, https://doi.org/10.1016/j.progsurf.2015.07.001.

[2] C. Gong, C. Huang, J. Miller, L. Cheng, Y. Hao, D. Cobden, J. Kim, R.S. Ruoff, R. M. Wallace, K. Cho, X. Xu, Y.J. Chabal, Metal Contacts on Physical Vapor Deposited Monolayer MoS 2, ACS Nano. 7 (2013) 11350–11357, https://doi.org/10.1021/nn4052138.

[3] Y. Xu, C.-Y. Hsieh, L. Wu, L.K. Ang, Two-dimensional transition metal dichalcogenides mediated long range surface plasmon resonance biosensors, J. Phys. D. Appl. Phys. 52 (2019), 065101, https://doi.org/10.1088/1361-6463/aaf0f7.

[4] D. Deng, K.S. Novoselov, Q. Fu, N. Zheng, Z. Tian, X. Bao, Catalysis with two-dimensional materials and their heterostructures, Nat. Nanotechnol. 11 (2016) 218–230, https://doi.org/10.1038/nnano.2015.340.

[5] T.A. Shifa, F. Wang, Y. Liu, J. He, Heterostructures Based on 2D Materials: A Versatile Platform for Efficient Catalysis, Adv. Mater. 31 (2019) 1804828, https://doi.org/10.1002/adma.201804828.

[6] K. Kato, H. Omoto, T. Tomioka, A. Takamatsu, Visible and near infrared light absorbance of Ag thin films deposited on ZnO under layers by magnetron sputtering, Sol. Energy Mater. Sol. Cells. 95 (2011) 2352–2356, https://doi.org/10.1016/j.solmat.2011.04.005.

[7] G. Zhao, S.M. Kim, S.-G. Lee, T.-S. Bae, C. Mun, S. Lee, H. Yu, G.-H. Lee, H.-S. Lee, M. Song, J. Yun, Bendable Solar Cells from Stable, Flexible, and Transparent Conducting Electrodes Fabricated Using a Nitrogen-Doped Ultrathin Copper Film, Adv. Funct. Mater. 26 (2016) 4180–4191, https://doi.org/10.1002/adfm.201600392.

[8] G. Zhao, W. Shen, E. Jeong, S.G. Lee, H.S. Chung, T.S. Bae, J.S. Bae, G.H. Lee, J. Tang, J. Yun, Nitrogen-Mediated Growth of Silver Nanocrystals to Form UltraThin, High-Purity Silver-Film Electrodes with Broad band Transparency for Solar Cells, ACS Appl. Mater. Interfaces. 10 (2018) 40901–40910, https://doi.org/10.1021/acsami.8b13377.

[9] W. Wang, M. Song, T.-S. Bae, Y.H. Park, Y.-C. Kang, S.-G. Lee, S.-Y. Kim, D.H. Kim, S. Lee, G. Min, G.-H. Lee, J.-W. Kang, J. Yun, Transparent Ultrathin Oxygen-Doped Silver Electrodes for Flexible Organic Solar Cells, Adv. Funct. Mater. 24 (2014) 1551–1561, https://doi.org/10.1002/adfm.201301359.

[10] C.T. Campbell, Metal films and particles on oxide surfaces: structural, electronic and chemisorptive properties, J. Chem. Soc. Faraday Trans. 92 (1996) 1435, https://doi.org/10.1039/ft9969201435.

[11] T. Michely, J. Krug, Islands, Mounds and Atoms, 1st ed., Springer-Verlag Berlin Heidelberg, Berlin, Heidelberg, 2004. https://doi.org/10.1007/978-3-642-18672-1.

[12] A. Anders, E. Byon, D.-H. Kim, K. Fukuda, S.H.N. Lim, Smoothing of ultrathin silver films by transition metal seeding, Solid State Commun. 140 (2006) 225–229, https://doi.org/10.1016/j.ssc.2006.08.027.

[13] M. Messaykeh, S. Chenot, P. David, G. Cabailh, J. Jupille, A. Koltsov, R. Lazzari, An In Situ and Real-Time Plasmonic Approach of Seed/Adhesion Layers: Chromium Buffer Effect at the Zinc/Alumina Interface, Cryst. Growth Des. 21 (2021) 3528–3539, https://doi.org/10.1021/acs.cgd.1c00299.

[14] A. Jamnig, N. Pliatsikas, G. Abadias, K. Sarakinos, On the effect of copper as wetting agent during growth of thin silver films on silicon dioxide substrates, Appl. Surf. Sci. 538 (2021), 148056, https://doi.org/10.1016/j.apsusc.2020.148056.

[15] A. Jamnig, N. Pliatsikas, G. Abadias, K. Sarakinos, Manipulation of thin metal film morphology on weakly interacting substrates via selective deployment of alloying species, J. Vac. Sci. Technol. A. 40 (2022), 033407, https://doi.org/10.1116/6.0001700.

[16] J. Bulíř, M. Novotný, J. Lančok, L. Fekete, J. Drahokoupil, J. Musil, Nucleation of ultrathin silver layer by magnetron sputtering in Ar/N2 plasma, Surf. Coatings Technol. 228 (2013) S86–S90, https://doi.org/10.1016/j.surfcoat.2012.08.021.

[17] J. Yun, H.-S. Chung, S.-G. Lee, J.-S. Bae, T.E. Hong, K. Takahashi, S.M. Yu, J. Park, Q. Guo, G.-H. Lee, S.Z. Han, Y. Ikoma, E.-A. Choi, An unexpected surfactant role of immiscible nitrogen in the structural development of silver nanoparticles: an experimental and numerical investigation, Nanoscale. 12 (2020) 1749–1758, https://doi.org/10.1039/C9NR08076G.

[18] J.M. Riveiro, P.S. Normile, J.P. Andrés, J.A. González, J.A. De Toro, T. Muñoz, P. Muñiz, Oxygen-assisted control of surface morphology in nonepitaxial sputter growth of Ag, Appl. Phys. Lett. 89 (2006), 201902, https://doi.org/10.1063/1.2388140.

[19] A. Jamnig, N. Pliatsikas, M. Konpan, J. Lu, T. Kehagias, A.N. Kotanidis, N. Kalfagiannis, D.V. Bellas, E. Lidorikis, J. Kovac, G. Abadias, I. Petrov, J. E. Greene, K. Sarakinos, 3D-to-2D Morphology Manipulation of Sputter-Deposited Nanoscale Silver Films on Weakly Interacting Substrates via Selective Nitrogen Deployment for Multifunctional Metal Contacts, ACS Appl. Nano Mater. 3 (2020) 4728–4738, https://doi.org/10.1021/acsanm.0c00736.

[20] N. Pliatsikas, A. Jamnig, M. Konpan, A. Delimitis, G. Abadias, K. Sarakinos, Manipulation of thin silver film growth on weakly interacting silicon dioxide substrates using oxygen as a surfactant, J. Vac. Sci. Technol. A. 38 (2020), 043406, https://doi.org/10.1116/6.0000244.

[21] R. Zapata, M. Balestrieri, I. Gozhyk, H. Montigaud, R. Lazzari, On the O 2 " Surfactant " Effect during Ag / SiO 2 Magnetron Sputtering Deposition : The Point of View of In Situ and Real-Time Measurements, (2023). https://doi.org/10.1021/acsami.3c05689.

[22] Z. Wang, S.A. Cohen, D.N. Ruzic, M.J. Goeckner, Nitrogen atom energy distributions in a hollow-cathode planar sputtering magnetron, Phys. Rev. E. 61 (2000) 1904–1911, https://doi.org/10.1103/PhysRevE.61.1904.

[23] A.V. Volynets, D.V. Lopaev, T.V. Rakhimova, A.A. Chukalovsky, Y.A. Mankelevich, N.A. Popov, A.I. Zotovich, A.T. Rakhimov, N 2 dissociation and kinetics of N(4 S) atoms in nitrogen DC glow discharge, J. Phys. D. Appl. Phys. 51 (2018), 364002, https://doi.org/10.1088/1361-6463/aad1ca.

[24] K. Sarakinos, J. Alami, S. Konstantinidis, High power pulsed magnetron sputtering: A review on scientific and engineering state of the art, Surf. Coatings Technol. 204 (2010) 1661–1684, https://doi.org/10.1016/j.surfcoat.2009.11.013.

[25] J. Colin, A. Jamnig, C. Furgeaud, A. Michel, N. Pliatsikas, K. Sarakinos, G. Abadias, In Situ and Real-Time Nanoscale Monitoring of Ultra-Thin Metal Film Growth Using Optical and Electrical Diagnostic Tools, Nanomaterials. 10 (2020) 2225, https://doi.org/10.3390/nano10112225.

[26] A. Arnoult, J. Colin, Magnification inferred curvature for real-time curvature monitoring, Sci. Rep. 11 (2021) 9393, https://doi.org/10.1038/s41598-021-88722-6.

[27] G.G. Stoney, The Tension of Metallic Films Deposited by Electrolysis, Proc. R. Soc. London A. 82 (1909) 172–175, https://doi.org/10.1098/rspa.1909.0021.

[28] G. Abadias, L. Simonot, J.J. Colin, A. Michel, S. Camelio, D. Babonneau, Volmer-Weber growth stages of polycrystalline metal films probed by in situ and real-time optical diagnostics, Appl. Phys. Lett. 107 (2015), 183105.

[29] L. Simonot, D. Babonneau, S. Camelio, D. Lantiat, P. Guérin, B. Lamongie, V. Antad, In situ optical spectroscopy during deposition of Ag:Si3N4 nanocomposite films by magnetron sputtering, Thin Solid Films. 518 (2010) 2637–2643, https://doi.org/10.1016/j.tsf.2009.08.005.

[30] C.M. Herzinger, B. Johs, W.A. McGahan, J.A. Woollam, W. Paulson, Ellipsometric determination of optical constants for silicon and thermally grown silicon dioxide via a multi-sample, multi-wavelength, multi-angle investigation, J. Appl. Phys. 83 (1998) 3323–3336, https://doi.org/10.1063/1.367101.

[31] A. Jamnig, D.G. Sangiovanni, G. Abadias, K. Sarakinos, Atomic-scale diffusion rates during growth of thin metal films on weakly-interacting substrates, Sci. Rep. 9 (2019) 6640, https://doi.org/10.1038/s41598-019-43107-8.

[32] C.A. Schneider, W.S. Rasband, K.W. Eliceiri, NIH Image to ImageJ: 25 years of image analysis, Nat. Methods. 9 (2012) 671–675, https://doi.org/10.1038/nmeth.2089.

[33] Picture Thresholding Using an Iterative Selection Method, IEEE Trans. Syst. Man. Cybern. 8 (1978) 630–632. https://doi.org/10.1109/TSMC.1978.4310039.

[34] F. Wooten, Optical Properties of Solids, 1st ed.,, Academic Press, New York, 1972 https://doi.org/10.1016/C2013-0-07656-6.

[35] J. Jokinen, J. Keinonen, P. Tikkanen, A. Kuronen, T. Ahlgren, K. Nordlund, Comparison of TOF-ERDA and nuclear resonance reaction techniques for range profile measurements of keV energy implants, Nucl. Instruments Methods Phys. Res. Sect. B Beam Interact. with Mater. Atoms. 119 (1996) 533–542, https://doi.org/10.1016/S0168-583X(96)00469-7.

[36] J.F. Ziegler, M.D. Ziegler, J.P. Biersack, SRIM – The stopping and range of ions in matter (2010), Nucl. Instruments Methods Phys. Res. Sect. B Beam Interact. with Mater. Atoms. 268 (2010) 1818–1823. https://doi.org/10.1016/j.nimb.2010.02.091.

[37] J. Carrey, J.-L. Maurice, Scaling laws near percolation during three-dimensional cluster growth: A Monte Carlo study, Phys. Rev. B. 65 (2002), 205401, https://doi.org/10.1103/PhysRevB.65.205401.

[38] J.M. Warrender, M.J. Aziz, Effect of deposition rate on morphology evolution of metal-on-insulator films grown by pulsed laser deposition, Phys. Rev. B. 76 (2007), 045414, https://doi.org/10.1103/PhysRevB.76.045414.

[39] B. Lü, L. Souqui, V. Elofsson, K. Sarakinos, Scaling of elongation transition thickness during thin-film growth on weakly interacting substrates, Appl. Phys. Lett. 111 (2017), 084101, https://doi.org/10.1063/1.4993252.

[40] V. Elofsson, B. Lü, D. Magnfält, E.P. Münger, K. Sarakinos, Unravelling the physical mechanisms that determine microstructural evolution of ultrathin Volmer-Weber films, J. Appl. Phys. 116 (2014), 044302, https://doi.org/10.1063/1.4890522.

[41] B. Lü, V. Elofsson, E.P. Münger, K. Sarakinos, Dynamic competition between island growth and coalescence in metal-on-insulator deposition, Appl. Phys. Lett. 105 (2014), 163107, https://doi.org/10.1063/1.4900575.

[42] S. Esch, M. Hohage, T. Michely, G. Comsa, Origin of oxygen induced layer-by-layer growth in homoepitaxy on Pt(111), Phys. Rev. Lett. 72 (1994) 518–521, https://doi.org/10.1103/PhysRevLett.72.518.

[43] See supporting information file for island size and aspect ratio distributions and XRD analysis, as well ToF-ERDA depth profiles and XPS high-resolution scans, (n. d.).

[44] I. Petrov, P.B. Barna, L. Hultman, J.E. Greene, Microstructural evolution during film growth, J. Vac. Sci. Technol. A Vacuum, Surfaces Film 21 (2003) S117–S128, https://doi.org/10.1116/1.1601610.

[45] D. Depla, R. De Gryse, Target voltage measurements during DC sputtering of silver in a nitrogen/argon plasma, Vacuum. 69 (2003) 529–536, https://doi.org/10.1016/S0042-207X(02)00602-4.

[46] J. Carrey, J.-L. Maurice, Transition from droplet growth to percolation: Monte Carlo simulations and an analytical model, Phys. Rev. B. 63 (2001), 245408, https://doi.org/10.1103/PhysRevB.63.245408.

[47] J.E. Greene, Thin Film Nucleation, Growth, and Microstructural Evolution, in: Handb. Depos. Technol. Film. Coatings, Elsevier, 2010: pp. 554–620. https://doi.org/10.1016/B978-0-8155-2031-3.00012-0.

[48] D. Depla, Chemical Stability of Sputter Deposited Silver Thin Films, Coatings. 12 (2022) 1915, https://doi.org/10.3390/coatings12121915.

[49] V. Gervilla, G.A. Almyras, B. Lü, K. Sarakinos, Coalescence dynamics of 3D islands on weakly-interacting substrates, Sci. Rep. 10 (2020) 2031, https://doi.org/10.1038/s41598-020-58712-1.

[50] R.N. Carter, M.J. Murphy, A. Hodgson, On the recombinative desorption of N2 from Ag(111), Surf. Sci. 387 (1997) 102–111, https://doi.org/10.1016/S0039-6028(97)00271-9.

[51] G.-C. Wang, L. Jiang, X.-Y. Pang, J. Nakamura, Cluster and Periodic DFT Calculations: The Adsorption of Atomic Nitrogen on M(111) (M = Cu, Ag, Au) Surfaces, J. Phys. Chem. B. 109 (2005) 17943–17950, https://doi.org/10.1021/jp0500034.